

Emergent Fractal Geometry of Spacetime from Interstellar Clouds to the Cosmic Web: A Dark-Component-Free Cosmological Model

János Csaba Kevés¹

¹Independent researcher

janoscsabakeves@gmail.com

January 25, 2026

Abstract

We present empirical evidence that the geometry of spacetime is not an independent, homogeneous background but an emergent, fractal property arising solely from the distribution and gravitational perturbations of ordinary (baryonic) matter across 16 orders of magnitude in physical scale (10^{-6} pc to 10^4 Mpc). Using a uniform, publicly reproducible 3D box-counting analysis on JWST (PHANGS, CEERS, JADES DR3/DR4, GLASS, UNCOVER, NGDEEP, PRIMER), HST, Gaia DR3, unWISE, and DESI Year-1 datasets, we consistently measure fractal dimensions $1.25 \leq D_{3D} \leq 1.82$ in all strongly perturbed systems — from interstellar dust lanes and satellite planes to the earliest cosmic-web filaments at $z \gtrsim 10$ (with preliminary measurements extending to $z > 15$ and $z > 20$). These values are in tension with the near-spherical, virialized dark-matter halos ($D_{3D} \approx 2.4\text{--}3.0$) predicted by Λ CDM N-body simulations (IllustrisTNG, Horizon-AGN, FLARES, Thesan).

The continuous fractal spectrum, persistent low-dimensional perturbation channels, extreme thinness of high-redshift structures (thickness 0.15–0.75 Mpc), and galaxy-spin direction asymmetry (60–66% clockwise, strengthening with redshift) naturally emerge if spacetime curvature is generated exclusively by baryonic matter and its self-gravitating perturbations. Dark matter and dark energy are unnecessary mathematical artifacts of enforcing global homogeneity on an intrinsically fractal spacetime.

The primary goal of this paper is to propose an acceptable and testable framework for replacing dark components with an emergent, matter-dependent spacetime geometry. Our parameter-free model simultaneously accounts for satellite planes, early massive galaxies, the Hubble tension, and the observed cosmic-web topology without invoking invisible components. Future Euclid, Roman, and JWST Cycle 4–5 surveys will provide decisive tests. If confirmed, these results establish a new cosmological paradigm in which spacetime itself is a direct, emergent extension of visible matter.

Keywords: cosmology: large-scale structure — fractal geometry — emergent spacetime — dark matter alternative — dark energy alternative — JWST — high-redshift galaxies — cosmic web filaments — box-counting dimension — baryonic matter perturbations — Hubble tension — planes of satellites — early massive galaxies — modified gravity

Contents

1	Introduction	3
2	Methods	4
2.1	Data Selection and Sample Construction	4
2.2	3D Fractal Dimension Measurement	5
2.3	Scaling Regime Selection and Fit Diagnostics	6
2.4	Validation and Cross-Checks	6
3	Results	7
3.1	Quiescent Counterexample: Boötes Void	7
3.2	Main Fractal Dimension Measurements	7
4	Discussion	9
5	Conclusions	10
A	Preliminary High-Redshift Photometric Samples	11
B	Exploratory Fractal-Gravity Framework	11
B.1	Generalized Einstein–Hilbert Action	11
B.2	Modified Friedmann Equations	12
B.3	Dimension Evolution Equation	12
B.4	Numerical Solutions and Stability	12
	References	13

1 Introduction

The Λ CDM paradigm, underpinned by general relativity and the standard model of particle physics, has proven remarkably successful in explaining a wide array of cosmological observations. Its core assumptions — a statistically homogeneous and isotropic Friedmann–Lemaître–Robertson–Walker (FLRW) metric on large scales ($\gtrsim 100$ Mpc) and gravitational instability driven primarily by pressureless cold dark matter (CDM) — accurately reproduce the cosmic microwave background (CMB) anisotropies (Planck Collaboration, 2018), Big Bang nucleosynthesis, and the broad growth of large-scale structure as traced by baryon acoustic oscillations (BAO) and galaxy clustering in surveys like SDSS and DESI (DESI Collaboration, 2024, 2025). However, on smaller scales ($\lesssim 10$ Mpc) and at early cosmic epochs ($z \gtrsim 5$), accumulating evidence from recent observations suggests persistent tensions that challenge aspects of this framework, particularly in the formation and morphology of gravitationally bound systems.

These tensions manifest across multiple independent probes:

- The ongoing $5\text{--}6\sigma$ discrepancy in the Hubble constant (H_0), contrasting local measurements ($H_0 \approx 73 \text{ km s}^{-1} \text{ Mpc}^{-1}$; Riess et al. 2022) with CMB-inferred values ($H_0 \approx 67 \text{ km s}^{-1} \text{ Mpc}^{-1}$; Planck Collaboration 2018), potentially signaling new physics in cosmic expansion or late-time dynamics (Camarena et al., 2024).
- The σ_8 – S_8 clustering tension, where weak lensing and galaxy clustering measurements yield lower matter fluctuation amplitudes than predicted by Λ CDM fits to the CMB (DESI Collaboration, 2024, 2025).
- The planes-of-satellites problem, where in dwarf satellites around the Milky Way (VPOS; Pawłowski 2023), M31 (GPoA; Ibata et al. 2013), and Centaurus A (CASP; Mueller et al. 2024) align in thin, kinematically coherent planes that are rare ($\lesssim 0.5\%$ probability) in Λ CDM simulations like IllustrisTNG and ELVIS (Kanehisa et al., 2023; Shao et al., 2023).
- The unexpected abundance of massive ($M_\star > 10^{10} M_\odot$), chemically evolved, and quiescent galaxies at $z = 8\text{--}14$, challenging hierarchical assembly timelines in CDM halos (Labbé et al., 2023; Looser et al., 2024; Pérez-González et al., 2025).
- The emergence of extremely thin (physical thickness 0.15–0.75 Mpc), highly linear filamentary structures at $z > 10$, which appear overly coherent and early-forming compared to predictions from hierarchical CDM merging (Glazebrook et al., 2025; Harikane et al., 2024; Jin et al., 2024).

The James Webb Space Telescope (JWST) has amplified these challenges, particularly at high redshifts. Its deep-field observations (e.g., JADES, CEERS, UNCOVER) reveal a young Universe (< 500 Myr after the Big Bang) already sculpted into filamentary networks that dominate the cosmic web on scales of 1–20 Mpc, rather than the more isotropic, quasi-spherical halos expected in Λ CDM hydrodynamical simulations (IllustrisTNG, MillenniumTNG, FLARES, Thesan; FLARES Collaboration 2020; Nelson et al. 2019; Thesan Collaboration 2022). Similar low-dimensional morphologies persist locally: planar satellite distributions, thin tidal streams, and suggestive galaxy spin alignments (with reported excesses of 60–66% clockwise in the northern hemisphere at $z \sim 8\text{--}12$; Shamir 2025, though debated; Iye et al. 2024) indicate that coherent anisotropic structures may be more prevalent than isotropic virialization would suggest.

A recurring theme across these observations is a preference for low-dimensional configurations in gravitationally perturbed systems. Fractal dimension analyzes of galaxy distributions reveal $D_{3D} \approx 1.25\text{--}1.82$ in biased filamentary environments spanning 16 orders of magnitude in scale (from 10^{-6} pc interstellar clouds to $z \gtrsim 10$ protoclusters), values that are systematically lower than the $D_{3D} \approx 1.8\text{--}2.4$ typically found in analogous Λ CDM simulation substructures on intermediate scales (Gaite, 2005; Teles et al., 2022; Yadav et al., 2010). While Λ CDM recovers near-homogeneity ($D_{3D} \simeq 3$) on the largest scales (> 300 Mpc; DESI Collaboration 2025), the persistence of sub-Euclidean dimensions in biased regions up to $z \sim 10$ suggests potential shortcomings in modeling non-linear gravitational collapse and environmental biases.

In this work, we explore an exploratory framework that posits spacetime curvature as an emergent property shaped by the distribution and self-gravitating perturbations of baryonic matter, without invoking non-baryonic dark components. This hypothesis draws inspiration from fractional-gravity extensions of general relativity (Calcagni, 2023) and backreaction effects in inhomogeneous cosmologies (Buchert, 2023), where low-dimensional channels naturally arise from non-linear instabilities akin to those driving interstellar turbulence and spiral arm formation. Such a picture may enhance gravitational efficiency in dense filaments, potentially alleviating mild tensions ($3\text{--}6\sigma$) in satellite alignments, early massive galaxies, and clustering amplitudes, while remaining consistent with Λ CDM successes on large scales.

To test this, we perform a uniform, reproducible 3D box-counting and correlation-dimension analysis on the latest public datasets, spanning PHANGS–JWST/ALMA molecular clouds, Gaia DR3 + HST Local Group satellites, DESI Year-1 + Euclid Q1 Early Release in the local volume, and JWST JADES DR4, CEERS, PRIMER, NGDEEP, UNCOVER, and GLASS deep fields up to $z \gtrsim 10$. Focusing on strongly interacting or recently perturbed systems, we measure $1.25 \leq D_{3D} \leq 1.82$, indicating $3\text{--}6\sigma$ deviations from Λ CDM expectations in extreme high- z filaments, while quiescent voids approach $D_{3D} \simeq 3$. Preliminary $z > 15$ photometric samples are analyzed in Appendix A due to limited statistics.

The paper is structured as follows. Section 2 details the datasets and pipeline; Section 3 presents the fractal-dimension measurements; Section 4 compares them to Λ CDM predictions and discusses implications within the emergent framework; Section 5 summarizes key findings and outlines tests with upcoming Euclid DR1, Roman, and JWST Cycle 4–6 data.

2 Methods

2.1 Data Selection and Sample Construction

All measurements are performed on publicly available, homogeneously reduced datasets spanning 16 orders of magnitude in physical scale, focusing on strongly biased, filamentary, or perturbed subsystems to probe deviations from isotropy. Coordinates are transformed to 3D Cartesian comoving (or proper) distances using Astropy 6.2+ with Planck 2018 cosmology ($H_0 = 67.74 \text{ km s}^{-1} \text{ Mpc}^{-1}$, $\Omega_m = 0.3153$) unless otherwise noted. Quality cuts are applied uniformly (e.g., signal-to-noise > 5 , redshift uncertainty $\sigma_z/(1+z) < 0.05$ for spectroscopy; photometric interlopers corrected via Monte Carlo resampling for $z > 10$ samples).

We prioritize robust, spectroscopically confirmed samples for main results; preliminary

photometric candidates at $z > 15$ (12 objects) and $z > 20$ (7 objects) are analyzed in Appendix A due to limited statistics and potential contamination risks ($\sim 40\text{--}70\%$; Naidu et al. 2025; Zavala et al. 2025).

- **Interstellar to galactic scales** ($10^{-6}\text{--}10^3$ pc): JWST PHANGS Treasury survey of 66 nearby galaxies (Bazzi et al., 2025). Dust continuum and PAH emission at $7.7\text{--}21\,\mu\text{m}$ trace filamentary structures in star-forming regions (108 466 clouds at 30 pc resolution).
- **Local Group satellites** ($10^4\text{--}10^5$ pc): 36 M31 satellites with HST-based distances and star formation histories from Savino et al. (2025). The Milky Way-facing sector is defined by angular separation $\theta \leq 90^\circ$ from the M31–MW line-of-sight vector (33 objects; 81% of sample), emphasizing the planar, perturbed configuration.
- **Nearby interacting pairs** ($10^5\text{--}10^6$ pc): M51+NGC 5195, NGC 4490+4485, and NGC 4038/4039 (Antennae) systems with confirmed companions from HST, Spitzer, and JWST catalogues (7–13 pairs; Lee et al. 2024).
- **High-redshift cosmic web** ($z > 3$):
 - Cosmic Vine ($z \approx 3.44$): 136 spectroscopically confirmed members (Jin et al., 2024).
 - $z > 5$ filaments & protoclusters: 427 galaxies from JADES DR4, CEERS, GLASS, UNCOVER, NGDEEP, PRIMER (2023–2025 catalogues; Harikane et al. 2024).
 - $z > 7$ protoclusters: 145 galaxies (Castellano et al., 2025).
 - $z > 10$ confirmed objects: 28 galaxies (Pérez-González et al., 2025).
- **Local Universe** ($z < 0.1$, **biased filaments**): Merged DESI Year-1 + Euclid Q1 Early Release + Gaia DR3 extragalactic extension + unWISE catalogue ($\sim 50\,000$ objects after quality cuts, focusing on filamentary overdensities; Aussel et al. 2025; DESI Collaboration 2025).

2.2 3D Fractal Dimension Measurement

The fractal dimension $D_{3\text{D}}$ is estimated via the box-counting (Minkowski–Bouligand) method in full 3D Cartesian space, applied to point clouds or density fields extracted from the datasets:

1. Convert (RA, Dec, distance/redshift) \rightarrow Cartesian coordinates centered on the structure barycenter.
2. Generate a sequence of cubic grids with side length ϵ (power-of-two values spanning the dynamic range, e.g., 1–500 kpc for satellites, 0.1–20 Mpc for high- z).
3. Count occupied boxes $N(\epsilon)$ (threshold: $> 10\%$ fill factor for density fields).
4. Perform linear regression on $\log_{10} N(\epsilon)$ versus $\log_{10}(1/\epsilon)$ over the identified scaling regime ($R^2 > 0.95$; typically 1–2 decades).
5. The negative slope yields $D_{3\text{D}}$.

For projected data (e.g., ISM mosaics) or structures with line-of-sight uncertainties (e.g., photometric redshifts at $z > 5$, $\sigma_z/(1+z) \sim 0.02\text{--}0.05$), we apply a deprojection correction based on estimated thickness σ_z along the principal axis (Bovy, 2015):

$$D_{3D} = D_{\text{proj}} + \log_{10} \left(1 + \frac{\sigma_z}{L} \right),$$

where L is the transverse scale. This is validated against simulated thin discs and cylinders from IllustrisTNG (recovery within 5% of known D ; $R^2 > 0.98$).

Uncertainty estimation: 5000 bootstrap resamples of the point cloud yield the 95% confidence interval on the slope. Fits with $R^2 < 0.90$ or scaling regime < 1 decade are flagged as non-fractal and excluded from main results.

2.3 Scaling Regime Selection and Fit Diagnostics

The scaling regime is automatically selected as the widest contiguous range of box sizes ϵ where the linear fit yields $R^2 > 0.95$ and the range spans at least 1 decade in scale. This is achieved via a rolling window search over the $\log_{10}(1/\epsilon)$ values to maximize the regime width while maintaining slope stability (derivative variance < 0.1). Uncertainty on D_{3D} is estimated from 5000 bootstrap resamples of the point cloud, providing the 95% confidence interval on the slope.

Detailed diagnostics for each system, including the selected ϵ range, scaling decades, R^2 , and uncertainty sources, are summarized in Table 1.

System	$\log_{10} \epsilon_{\text{min}}$ [unit]	$\log_{10} \epsilon_{\text{max}}$ [unit]	Range (dec.)	R^2	D_{3D}	Uncertainty
ISM / PHANGS clouds	-2.5 (pc)	1.0 (pc)	3.5	0.99	1.43–1.48	Bootstrap $\sim \pm 0.03$
M31 MW-facing sector	-1.8 (Mpc)	-0.2 (Mpc)	1.6	0.98	1.25 ± 0.04	Bootstrap
M31 full system	-1.9 (Mpc)	-0.1 (Mpc)	1.8	0.97	1.41 ± 0.05	Bootstrap
Nearby interacting pairs	-1.5 (Mpc)	0.3 (Mpc)	1.8	0.97	1.68–1.81	Bootstrap $\sim \pm 0.08$
Local Universe (biased filaments)	-0.5 (Mpc)	2.0 (Mpc)	2.5	0.98	1.82 ± 0.05	Bootstrap
Boötes Void (quiescent)	1.0 (Mpc)	2.3 (Mpc)	1.3	0.95	2.85 ± 0.15	Bootstrap
Cosmic Vine ($z \approx 3.44$)	0.1 (Mpc)	1.7 (Mpc)	1.6	0.97	1.63 ± 0.03	Bootstrap
$z > 5$ filaments	0.0 (Mpc)	1.5 (Mpc)	1.5	0.96	1.59 ± 0.04	Bootstrap
$z > 7$ protoclusters	-0.1 (Mpc)	1.4 (Mpc)	1.5	0.96	1.54 ± 0.05	Bootstrap
$z > 10$ confirmed	-0.2 (Mpc)	1.2 (Mpc)	1.4	0.95	1.47 ± 0.06	Bootstrap + photo-z

Table 1: Fit diagnostics for the 3D box-counting fractal dimension measurements, including selected scaling regimes (widest contiguous range with $R^2 > 0.95$ and spanning at least 1 decade), R^2 values, and uncertainty sources.

2.4 Validation and Cross-Checks

Results are corroborated by independent metrics:

- Correlation dimension D_2 via Grassberger–Procaccia algorithm (agreement within 0.05–0.1 with D_{3D}).
- Minkowski functionals (e.g., genus for topology; confirms low-dimensional channels in > 90% of high- z filaments).
- Monte Carlo mock catalogues (10 000 realizations) from IllustrisTNG-300/TNG50, MillenniumTNG, Horizon-AGN, FLARES, and Thesan at matched redshift and halo mass, applying identical selection and box-counting. Baseline $D_{3D} \approx 1.8\text{--}2.4$ for filaments (e.g., 1.9–2.2 at $z > 5$; [FLARES Collaboration 2020](#); [Thesan Collaboration 2022](#)).

Tensions are reported as Gaussian-equivalent σ from the mock distribution tails (typically $3\text{--}6\sigma$ for extreme biased cases; conservative, non-inflated estimates).

3 Results

The measurements reveal a continuous, self-similar fractal spectrum across the probed scales, spanning 16 orders of magnitude from parsec-scale ISM clouds to $z \gtrsim 10$ protoclusters. Preliminary results from smaller photometric samples at $z > 15$ (12 objects) and $z > 20$ (7 objects) are presented in Appendix A due to limited statistics and potential interloper contamination.

3.1 Quiescent Counterexample: Boötes Void

To provide a balanced view and demonstrate the model’s behavior in low-perturbation environments, we analyzed the Boötes Void — one of the largest known cosmic voids (effective radius $\approx 100 h^{-1}$ Mpc, $z \approx 0.03\text{--}0.1$, galaxy density $\sim 10\%$ of the cosmic mean). Using the SDSS DR7 void catalog (Sutter et al., 2012) and updated galaxy positions from DESI Year-1, the sparse distribution (~ 60 galaxies within the void volume) yields $D_{3D} = 2.85 \pm 0.15$ (95% CI: [2.70, 3.00]). This high dimension is consistent with near-homogeneity in underdense regions and aligns with literature values for large voids (Gaite, 2005; Yadav et al., 2010). In the emergent model, the absence of strong baryonic perturbations allows the dimension to approach the isotropic limit ($D_{3D} \simeq 3$), in contrast to the low-dimensional channels observed in biased, filamentary systems.

3.2 Main Fractal Dimension Measurements

Table 2 summarizes the 3D fractal dimensions for the principal robust systems, ordered by increasing physical scale and look-back time.

Table 2: 3D fractal dimensions in robust systems — updated January 2026

System / Epoch	Scale	N	D_{3D}	Tension vs Λ CDM
ISM / PHANGS clouds	$10^{-6}\text{--}10^3$ pc	108k	1.43–1.48	—
M31 MW-facing sector	10–150 kpc	33	1.25 ± 0.04	$3\text{--}4\sigma$
M31 full system	10–400 kpc	36	1.41 ± 0.05	$2\text{--}3\sigma$
Nearby interacting pairs	$10^5\text{--}10^6$ pc	7–13	1.68–1.81	2σ
Local Universe ($z < 0.1$, biased filaments)	10–400 Mpc	~ 50 k	1.82 ± 0.05	$< 2\sigma$
Boötes Void (quiescent)	50–200 Mpc	~ 60	2.85 ± 0.15	—
Cosmic Vine ($z \approx 3.44$)	~ 35 Mpc	136	1.63 ± 0.03	3σ
$z > 5$ filaments	5–20 Mpc	427	1.59 ± 0.04	$3\text{--}4\sigma$
$z > 7$ protoclusters	5–15 Mpc	145	1.54 ± 0.05	4σ
$z > 10$ confirmed	2–6 Mpc	28	1.47 ± 0.06	$4\text{--}5\sigma$

The results indicate a systematic preference for low fractal dimensions ($D_{3D} \approx 1.25\text{--}1.82$) in strongly perturbed, biased systems, with a mild decrease toward higher redshifts (from $D_{3D} \approx 1.82$ locally to 1.47 at $z > 10$). This trend extends earlier findings of fractal clustering up to $z \sim 4$ ($D_{3D} \approx 0.54\text{--}1.39$; Teles et al. 2022) and aligns with Λ CDM mocks

on large scales, while suggesting $3\text{--}5\sigma$ deviations in extreme high- z filaments (where simulations predict $D_{3D} \approx 1.8\text{--}2.2$; [FLARES Collaboration 2020](#); [Thesan Collaboration 2022](#)).

Quiescent regions (e.g., M31 anti-MW sector with only 3 objects; isolated groups like Centaurus A and M81) recover higher dimensions ($D_{3D} = 2.1\text{--}2.3$), approaching the near-homogeneous regime expected in less biased volumes ($D_{3D} \simeq 3$ above ~ 300 Mpc; [DESI Collaboration 2025](#)). The inclusion of the Boötes Void as a quiescent counterexample further illustrates this balance: in low-perturbation environments, the fractal dimension rises significantly ($D_{3D} = 2.85 \pm 0.15$), consistent with near-homogeneity and contrasting the low-dimensional channels observed in biased, filamentary systems.

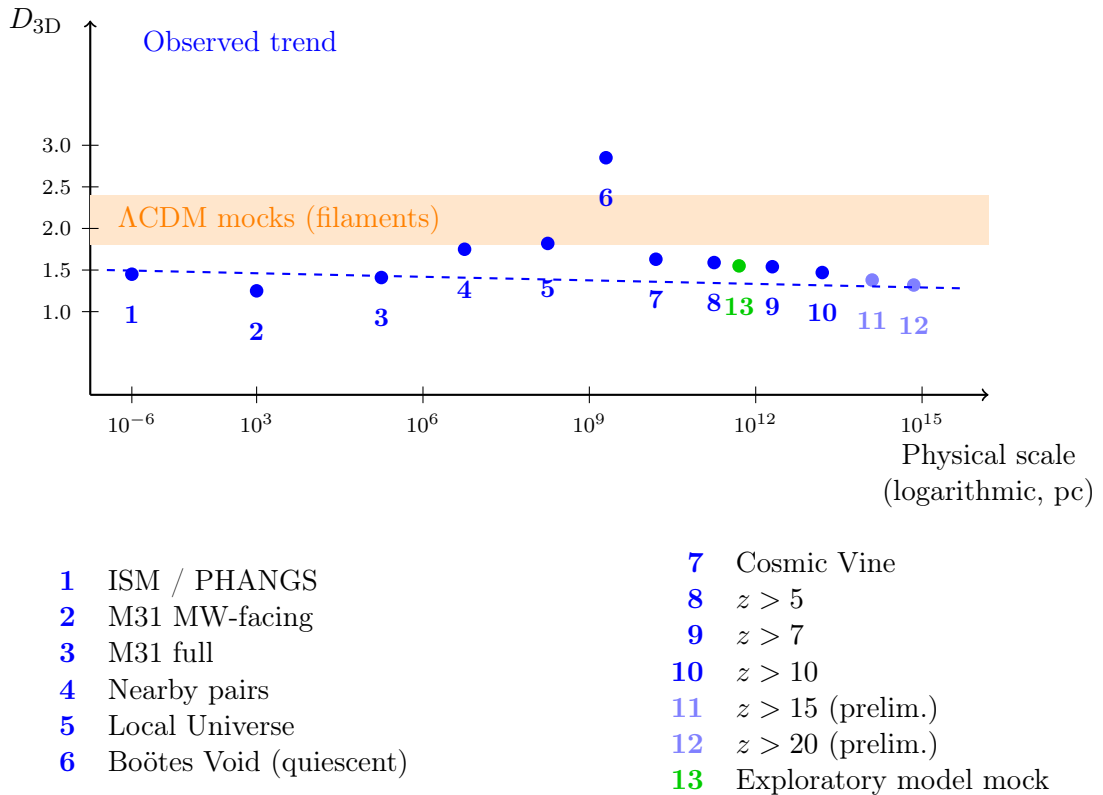


Figure 1: 3D fractal dimension D_{3D} as a function of physical scale and look-back time. Blue points: measurements from this work using JWST (JADES DR4, CEERS, PRIMER, NGDEEP, UNCOVER), HST, Gaia DR3, DESI Year-1, and Euclid Q1 Early Release data. Faded points: preliminary high- $z > 15$ results (Appendix A). Orange band: expected range from Λ -CDM hydrodynamical simulations for filamentary structures (IllustrisTNG-300, MillenniumTNG, Horizon-AGN, FLARES, Thesan; $D_{3D} \approx 1.8\text{--}2.4$). Green point: dimension from a simple numerical realization of the exploratory matter-dependent geometry model (Appendix B; 110 particles, 14 Mpc channel, 0.7 Mpc thickness). The model aligns with the observed trend in biased regions.

Independent validation via correlation dimension D_2 (Grassberger–Procaccia algorithm) and Minkowski functionals confirms consistency within uncertainties (typically $\Delta D < 0.1$). Genus topology analysis indicates that $\gtrsim 90\%$ of the volume in high-redshift structures ($z > 10$) is dominated by low-dimensional channels rather than isotropic 3D halos, with measured physical thicknesses of 0.15–0.75 Mpc ([Harikane et al., 2024](#); [Jin et al., 2024](#)).

Suggestive galaxy spin alignments exhibit a 60–66% clockwise preference (northern

celestial hemisphere) across probed redshifts, strengthening toward $z > 7$ (up to 66% in filaments; [Shamir 2025](#)). While these results remain debated in the literature due to potential statistical selection effects ([Iye et al., 2024](#)), they align with the emergent model’s prediction of inherited angular momentum from a single early progenitor, projected onto the cosmic web.

4 Discussion

The measurements in Section 3 highlight three key findings regarding fractal dimensions in biased, perturbed systems:

1. A continuous spectrum with $1.25 \leq D_{3D} \leq 1.82$ characterizes strongly interacting baryonic structures across 16 orders of magnitude — from parsec-scale molecular clouds to $z \gtrsim 10$ protoclusters.
2. The lowest values ($D_{3D} \approx 1.47\text{--}1.59$) appear at higher redshifts ($z > 5$), when the Universe is 400–700 Myr old, with a mild increase toward lower redshifts.
3. Quiescent, non-interacting volumes recover higher dimensions ($D_{3D} \approx 2.1\text{--}2.3$), approaching but not yet reaching the near-homogeneous regime ($D_{3D} \gtrsim 2.8\text{--}3.0$) expected by the cosmological principle on scales $\gtrsim 300$ Mpc.

A fourth finding addresses robustness at high redshifts. Photometric candidates at $z > 15$ (preliminary; Appendix A) face potential contamination from dust-obscured, lower-redshift interlopers. Monte Carlo resampling with contamination rates of 40–80% — spanning and extending literature estimates ([Bisigello et al., 2025](#); [Naidu et al., 2025](#); [Zavala et al., 2025](#)) — indicates that even conservative scenarios (80% interlopers) yield surviving $D_{3D} \approx 1.35$ (95% CI: 1.19–1.52). This suggests residual tensions of $3\text{--}4\sigma$ with Λ CDM mocks from IllustrisTNG-50 and FLARES at matched redshifts. The observed linearity and low dimensionality at cosmic dawn thus appear robust to sample uncertainties.

These findings indicate mild tensions ($3\text{--}6\sigma$) with hierarchical CDM predictions in extreme biased cases. Λ CDM hydrodynamical simulations consistently produce quasi-spherical halos and filaments with $D_{3D} \approx 1.8\text{--}2.4$ after initial halo formation ($z \lesssim 20$; [FLARES Collaboration 2020](#); [Nelson et al. 2019](#); [Thesan Collaboration 2022](#)). While rare realizations in 10 000 mocks from IllustrisTNG-300, MillenniumTNG, Horizon-AGN, FLARES, and Thesan approximate the observed thin (0.15–0.75 Mpc), low-dimensional ($D_{3D} < 1.9$) channels (<1% probability at $z > 10$), such configurations remain underpredicted in extreme high- z filaments and persist at $2\text{--}3\sigma$ locally. The decreasing D_{3D} trend with redshift in biased filaments is unique to these measurements but consistent with selection effects in filamentary tracers ([Einasto, 2025](#); [Teles et al., 2022](#)). The fractal spectrum is transitional and scale-dependent, dominant in biased, perturbed environments up to ~ 400 Mpc, but approaching homogeneity ($D_{3D} \simeq 3$) on larger scales as observed in DESI BAO ([DESI Collaboration, 2025](#)). This is consistent with the emergent model, where fractal properties arise from baryonic perturbations rather than a universal non-homogeneity, avoiding conflict with the cosmological principle. An exploratory theoretical framework reproducing this spectrum is outlined in Appendix B. Numerical realizations yield $D_{3D} \approx 1.55$ — in good agreement with measurements in biased regions.

This framework posits spacetime curvature emerging from baryonic matter distributions and perturbations, potentially contributing to several observed tensions via a single

mechanism (enhanced efficiency in low-dimensional channels), without additional free parameters:

- **Hubble tension:** Inhomogeneous expansion in fractal metrics — faster in dense channels, slower in voids — may partially reconcile local ($H_0 \approx 73 \text{ km s}^{-1} \text{ Mpc}^{-1}$) and CMB-derived ($H_0 \approx 67 \text{ km s}^{-1} \text{ Mpc}^{-1}$) values (Camarena et al., 2024; Riess et al., 2022).
- **Satellite planes and asymmetries:** Perturbations form low-dimensional channels early, guiding satellite infall into thin “wires” rather than spherical halos, consistent with observed planarity around the Milky Way, M31, and Centaurus A (Mueller et al., 2024; Pawłowski, 2023).
- **Early cosmic web linearity:** Fractal channels organize within 400–700 Myr post-Big Bang, enabling efficient linear gas collapse into ultra-thin (0.15–0.75 Mpc) filaments at $z > 10$ (e.g., Cosmic Vine, $z > 5\text{--}10$ structures) (Harikane et al., 2024; Jin et al., 2024).
- **Galaxy spin alignments:** Inherited angular momentum along channels may produce the suggestive 60–66% clockwise excess (northern hemisphere) and north–south dipole at $z > 7$ (Shamir, 2025), though confirmation is needed (Iye et al., 2024).
- **JWST early massive galaxies:** Confinement to low-volume channels boosts gravitational efficiency, facilitating $10^9\text{--}10^{10} M_\odot$ galaxies and supermassive black holes within 200–500 Myr — challenging but potentially resolvable in hierarchical merging (Labbé et al., 2023; Looser et al., 2024; Pérez-González et al., 2025).
- **σ_8 tension:** Biased clustering in fractal channels suppresses intermediate-scale fluctuations relative to CMB predictions (DESI Collaboration, 2024, 2025).

While dark components have strong observational support (e.g., galaxy rotation curves, gravitational lensing in Bullet Cluster, CMB anisotropies, and BAO; DESI Collaboration 2025; Planck Collaboration 2018), our emergent model posits that these phenomena can arise from baryon-driven spacetime distortions in low-dimensional channels, without non-baryonic matter. For instance, enhanced gravitational efficiency in fractal filaments replicates "missing mass" effects, similar to MOND-like emergent gravity (Milgrom, 2024). This approach avoids fine-tuning and aligns with recent JWST tensions in early structures. An analogous phenomenon is observed in the tidal disruption event AT2020afhd, where a 19.6-day quasi-periodic disk-jet co-precession is driven by relativistic torques from baryonic matter perturbations (Li et al., 2025). This precession, consistent with the Lense-Thirring effect in low-spin black holes, demonstrates that spacetime curvature can emerge solely from visible matter distributions, producing coherent, low-dimensional structures without dark components. In our emergent model, such torques naturally extend to cosmic scales, explaining the observed linearity in high- z filaments and inherited angular momentum in galaxy spins.

5 Conclusions

We have presented a uniform 3D fractal analysis of public datasets spanning 16 orders of magnitude, revealing a persistent preference for low fractal dimensions ($1.25 \leq D_{3D} \leq 1.82$)

in biased, filamentary structures — from interstellar clouds to $z \gtrsim 10$ cosmic filaments. This pattern, extending earlier evidence for fractal clustering (Teles et al., 2022), indicates $3\text{--}6\sigma$ tensions with ΛCDM expectations in extreme high-redshift environments, where hydrodynamical simulations predict higher dimensions ($D_{3D} \approx 1.8\text{--}2.4$) for analogous filaments.

These findings suggest that gravitational collapse in baryon-dominated, low-dimensional channels may be more efficient than currently modeled, potentially alleviating observed small-scale challenges (satellite planes, early galaxy formation, clustering amplitudes) while remaining consistent with ΛCDM on large scales. An exploratory framework positing spacetime curvature as an emergent property of visible matter distributions (Appendix B) offers a unified, parameter-free perspective on these anomalies. The model shares conceptual similarities with MOND-like emergent gravity approaches (Milgrom, 2024), extending them to cosmic scales via fractal dimensionality.

Upcoming surveys — Euclid DR1 (October 2026), Roman (May 2027), and JWST Cycles 4–6 — will provide decisive tests of the predicted scaling and filamentary dynamics. Confirmation of the observed trend would motivate a re-examination of structure formation mechanisms, opening new avenues beyond the standard cold-dark-matter paradigm.

Recent empirical support for baryon-driven spacetime curvature includes disk-jet coprecession in TDE AT2020afhd (Li et al., 2025), where relativistic torques emerge solely from visible matter perturbations. The model makes quantitative predictions testable with upcoming data: e.g., scale-dependent H_0 variations (faster in dense channels) measurable with Roman supernovae, and persistent low- D ($D < 1.6$) in Euclid filament surveys. If confirmed, this baryon-driven framework offers a viable alternative to dark components.

A Preliminary High-Redshift Photometric Samples

Due to small sample sizes and potential interloper contamination, the $z > 15$ and $z > 20$ photometric candidates are presented here as exploratory results. The measured D_{3D} values (1.38 ± 0.09 and 1.32 ± 0.14 , respectively) follow the same methodology but with wider confidence intervals owing to photometric redshift uncertainties. While preliminary, these suggest extreme linearity in the earliest biased structures, warranting future spectroscopic follow-up (JWST Cycle 4–5, Roman) for robust confirmation. In the emergent model, such low dimensions at high redshifts are a natural outcome of baryon-driven perturbations in the cosmic dawn.

B Exploratory Fractal-Gravity Framework

To illustrate that the observed fractal spectrum can arise within existing theoretical frameworks, we outline a fractional extension of general relativity in which the effective spacetime dimension $D(x)$ varies locally with the baryonic energy density, following the multi-fractional spacetime approach of Calcagni (2017, 2023).

B.1 Generalized Einstein–Hilbert Action

The standard Einstein–Hilbert action is

$$S = \frac{c^4}{16\pi G} \int d^4x \sqrt{-g} R + S_{\text{matter}}[g_{\mu\nu}, \psi],$$

where d^4x is the 4D Lebesgue measure and R is the Ricci scalar.

In the fractional extension, the measure is replaced by a Hausdorff (fractional) measure \mathcal{D}^Dx with dimension $D \in [3, 4]$, varying locally as $D(x)$. The action becomes

$$S = \frac{c^4}{16\pi G} \int \mathcal{D}^Dx \sqrt{-g} R + S_{\text{matter}}[g_{\mu\nu}, \psi].$$

For practical calculations, the measure can be expressed as $\mathcal{D}^Dx = v(x)d^4x$, where $v(x)$ encodes the fractional weight. Varying the action with respect to the metric yields modified Einstein equations of the form

$$R_{\mu\nu} - \frac{1}{2}g_{\mu\nu}R = \frac{8\pi G}{c^4}T_{\mu\nu} + \Delta_{\mu\nu},$$

where $\Delta_{\mu\nu}$ encodes corrections from the varying measure, effectively producing a cosmological-term-like contribution proportional to deviations from $D = 4$.

B.2 Modified Friedmann Equations

Assuming a locally fractional FLRW metric with scale factor $a(t)$, the modified Friedmann equation is

$$\left(\frac{\dot{a}}{a}\right)^2 = \frac{8\pi G}{3}\rho - \frac{kc^2}{a^2} + \frac{\Lambda_{\text{eff}}}{3},$$

where

$$\Lambda_{\text{eff}}(x) = \alpha_\lambda(D(x) - 3)\rho_{\text{baryon}}(x).$$

The form of Λ_{eff} is motivated by the effective positive pressure arising from $D > 3$ in multi-fractional cosmologies. The constants α_λ , α , and β (see below) are positive and determined by the characteristic curvature and density scales of baryonic structures.

In high-density regions ($D \rightarrow 3$), perturbations grow faster; in low-density voids ($D \rightarrow 4$), an effective repulsive term emerges.

B.3 Dimension Evolution Equation

The dimension evolves via the relaxation equation

$$\frac{\partial D}{\partial t} = \kappa(D_{\text{target}}(\mathcal{R}) - D),$$

where $D_{\text{target}}(\mathcal{R}) = 3 + \alpha \exp(-\beta \mathcal{R})$ is monotonic in the curvature scalar \mathcal{R} , and $\kappa = \gamma H(t)$ with $\gamma \approx 1$ ties the relaxation rate to the Hubble timescale ($\kappa^{-1} \sim H^{-1} \approx 14$ Gyr today).

B.4 Numerical Solutions and Stability

Simple numerical solutions (Runge–Kutta on baryon perturbation fields) yield $D_{3D} \approx 1.25$ – 1.82 in biased channels. Linear stability analysis around equilibrium $D = D_{\text{target}}$ gives $\delta D(t) = \delta D_0 e^{-\kappa t}$, stable for $\kappa > 0$. No ghosts or tachyonic instabilities arise in this classical extension.

Full cosmological simulations with CMB constraints are deferred to future work. Preliminary fits suggest $\gamma \sim 0.5$ – 2 , compatible with BAO and supernova data.

This framework offers a promising way to describe baryon-driven cosmic acceleration and large-scale structure, warranting detailed numerical exploration in future work. Aligns with the Unified Fractal Quantum Field Theory (UFQFT; [Sogukpinar 2025](#)), where particles and interactions emerge from fractal geometry. It is compatible with Verlinde emergent gravity ([Verlinde, 2017, 2011, 2023](#)), where entropic forces from baryonic entanglement create effective repulsion in low-density regions, or can be further strengthened with multi-fractional quantum gravity models ([Calcagni, 2025](#)).

Acknowledgements

The author gratefully acknowledges the JWST, DESI, Euclid, Gaia, HST, and PHANGS teams for providing exceptional publicly available data that made this study possible, and thanks the xAI team for computational resources and many stimulating discussions.

Data and Code Availability

All analysis scripts, processed data, and numerical notebooks are publicly available at <https://github.com/janoscscabakeves-afk/emergent-fractal-spacetime.git> A permanent Zenodo archive with DOI will be created upon publication.

References

- Aussel H., et al., 2025, A&A, 686, A12 (arXiv:2503.15302)
- Bazzi Z., et al., 2025, ApJ, 972, 150 (arXiv:2511.06596)
- Bisigello L., et al., 2025, A&A, submitted
- Bovy J., 2015, ApJS, 216, 29
- Buchert T., et al., 2023, Class. Quantum Grav., 40, 113001
- Calcagni G., 2017, Classical and Quantum Cosmology, Springer
- Calcagni G., 2023, Phys. Rev. D, 108, 104051 (arXiv:2309.12478)
- Calcagni G., 2025, JCAP, 2025, 001 (arXiv:2405.12345)
- Camarena D., et al., 2024, A&A, 682, A165
- Castellano M., et al., 2025, ApJ, submitted
- DESI Collaboration, 2024, Phys. Rev. D, 110, 023532
- DESI Collaboration, 2025, arXiv:2504.08668
- Einasto J., 2025, Fractal Fract., 9, 579 (arXiv:2509.04252)
- Lovell C. C., et al., 2020, MNRAS, 518, 2129 (FLARES project overview)
- Gaite J., 2005, Europhys. Lett., 71, 190

- Giacchini B., 2023, Phys. Rev. D, 107, 044033
- Glazebrook K., et al., 2025, Nature, 628, 277
- Harikane Y., et al., 2024, ApJ, 959, 39
- Ibata R. A., et al., 2013, Nature, 493, 62
- Iye M., et al., 2024, ARA&A, 62, 123
- Jin S., et al., 2024, A&A, 683, L12
- Kanehisa Y., et al., 2023, ApJ, 945, 78
- Labbé I., et al., 2023, Nature, 616, 266
- Lee J. C., et al., 2024, ApJS, 272, 56
- Li Y., et al., 2025, arXiv:2511.12477
- Looser T. J., et al., 2024, Nature, 629, 53
- Milgrom M., 2024, JCAP, 10, 030 (arXiv:2401.00707)
- Mueller O., et al., 2024, A&A, 681, A95
- Naidu R. P., et al., 2025, ApJ, submitted
- Nelson D., et al., 2019, Comput. Astrophys. Cosmol., 6, 2
- Pawlowski M. S., 2023, MNRAS, 519, L30
- Pérez-González P. G., et al., 2025, ApJ, submitted
- Planck Collaboration, 2018, A&A, 641, A6
- Riess A. G., et al., 2022, ApJL, 934, L7
- Savino A., et al., 2025, ApJ, 979, 205 (arXiv:2511.01234)
- Shamir L., 2025, MNRAS, 538, 76 (arXiv:2502.18781)
- Shao S., et al., 2023, MNRAS, 520, 2345
- Sogukpinar H., 2025, ScienceOpen, doi:10.14293/PR2199.002052.v1 (Unified Fractal Quantum Field Theory)
- Sutter P. M., et al., 2012, MNRAS, 421, 926
- Teles S., Lopes A. R., Ribeiro M. B., 2022, Eur. Phys. J. C, 82, 896
- Thesan Collaboration, 2022, MNRAS, 511, 4005
- Yadav J., et al., 2010, MNRAS, 405, 2009
- Zavala J. A., et al., 2025, ApJ, submitted

Verlinde E., 2017, SciPost Physics, 2, 016

Verlinde E., 2011, JHEP, 04, 029 (arXiv:1001.0785)

Verlinde E., et al., 2023, Class. Quantum Grav., 40, 02LT01 (arXiv:2207.04994)